M3LW-22OR0402028

Light Water Reactor Sustainability Program

Electrochemical probing of microstructural heterogeneities in irradiated and deformed stainless steel

September 2022

U.S. Department of Energy
Office of Nuclear Energy

M3LW-22OR0402028

Electrochemical probing of microstructural heterogeneities in irradiated and deformed stainless steel

Sina Shahrezaei ([1]), Xin Chen ([1]), Maxim Gussev ([2]), Gaurav Sant ([1])

[1] University of California, Los Angeles, CA, USA
[2] Oak Ridge National Laboratory, Oak Ridge, TN, USA

September 2022

Prepared for the
U.S. Department of Energy
Office of Nuclear Energy

EXECUTIVE SUMMARY

Overview: Irradiation assisted stress corrosion cracking (IASCC) in nuclear components amounts to higher energy production cost and reduction in productivity of the reactor during the repair period. IASCC is a multifaceted problem comprising various phenomena operating simultaneously, making it challenging to exactly describe the full spectra of the phenomenon mechanistically. Influence of the irradiation is attributed to the acceleration of stress corrosion cracking (SCC) phenomenon with changes to both material properties and water chemistry due to irradiation contributing to this acceleration. This work identifies the role of irradiation induced microstructural evolution on corrosion behavior of austenitic stainless steel (SS) and its potential implications on IASCC. Utilizing a multiscale and multimodal approach, the local electrochemical behavior, microstructure, and surface morphology of ion irradiated 304L SS before and after deformation was investigated. An increase in corrosion current, corrosion potential, and a decrease in impedance was observed in post ion irradiated specimens. Scanning electrochemical microscopies revealed an increase in corrosion susceptibility near strain heterogeneities known as dislocation channels (DCs). The present results indicate the contribution of irradiation induced microstructural defects on local surface accelerating corrosion rate during crack initiation and growth in light water reactors (LWR) environments.

Implications: Our approach improve towards understanding IASCC by differentiating corrosion contributions from irradiation, deformation, and the integrated impacts from the two. The present work develops methodologies that can capture the subtle differences in the local electrochemical behavior of surfaces when intersecting irradiation and deformation induced defects along the new surfaces created by an advancing crack.

ACKNOWLEDGEMENTS

The authors acknowledge financial support for this research from the U.S. Department of Energy's Light Water Reactor Sustainability (LWRS) Program Materials Research Pathway (MRP) through the Oak Ridge National Laboratory operated by UT-Battelle LLC (Contract #: 4000154999). The contents of this paper reflect the views and opinions of the authors who are responsible for the accuracy of data presented. This research was carried out in the Laboratory for the Chemistry of Construction Materials (LC^2) and the California Nanosystems Institute at UCLA. As such, the authors gratefully acknowledge the support that has made these facilities and their operations possible. The authors acknowledge Dr. Marta Pozuelo for her help with gathering and analyzing transmission electron microscopy (TEM) data.

CONTENTS

FIGURE CAPTIONS

TABLE CAPTION

Electrochemical probing of microstructural heterogeneities in irradiated and deformed stainless steel

1. Introduction

Nuclear energy, a low-carbon power source, amounts to 10 percent of global electricity generation with many power plants under construction or planned for future construction[1]. Irradiation assisted stress corrosion cracking (IASCC) of internal components of light water reactors (LWRs) is one of the major contributors to maintenance costs, operational delays, lifespan, and operational safety of aging reactors. IASCC is a multifaceted problem comprising various mechanisms (e.g., irradiation damage, mechanical deformation, and electrochemical degradation) effecting simultaneously, making it challenging to be understood, predicted, and prevented.

Influence of the irradiation is attributed to the acceleration of SCC phenomenon with changes to both the material and water chemistry contributing to this acceleration. Radiation effects on the material side includes continuous changes to the microstructure and microchemical compositional heterogeneities leading to formation of dislocation loops and networks, voids and/or bubbles, precipitates, and radiation induced segregation (RIS)[2]. With increase in radiation dose, the radiation hardened microstructure impedes dislocation motion where the deformation mode of the alloy changes from homogeneous to heterogenous. Plastic deformation localizes in dislocation channels (DCs) that typically span the full length of a grain and terminates at grain boundaries (GBs). IASCC has been shown to strongly correlate with the DC formation[3]. It is speculated that, at stresses below the yield strength of the alloy, DC can propagate onto the surface causing disruption to the passivation film leading to increase in local corrosion rate[4]. Therefore, it is feasible to bridge IASCC initiation to surface corrosion activities via electrochemical means.

Essentially, the enhancement in corrosion performance of DCs can be attributed to an elevated chemical/electrochemical energy of their defected microstructure. Introduction of defects such as point defect clusters and dislocations into the lattice of a metal results in dilatational strain that changes the energy landscape of those defects [5]. Lattice deformation results in changes to the electron work function, the surface charge of metal and the structure of the double electrochemical layer, therefore directly influencing the electrochemical behavior of metals [6,7]. The combination of irradiation and deformation induced defects on the newly formed surfaces during crack propagation or DC propagation into the surface is expected to impact corrosion behavior at these sites. Empirically, IASCC in LWR in-service condition is usually signified by the increase in corrosion potential [8]; however, studies on inherent electrochemical changes and their causes have not been established. In this work, we aim to attribute the IASCC events to the microstructural and electrochemical evolution of nuclear components, and by using spatially resolved electrochemical approaches, we use simplified indicators to untangle the multifaceted causes for IASCC.

Here, we have investigated changes in corrosion behavior of ion irradiated 304L stainless steel utilizing a combination microstructural and local electrochemical characterization on irradiated, and irradiated and deformed 304L stainless steel. Utilizing a combination of electrochemical micro-cell technique based on glass micro-capillaries and light microscopy[9], electrochemical impedance spectroscopy (EIS) and potentiodynamic polarization measurements were locally performed on ion irradiated and deformed microstructures. To correlate the resulting electrochemical behavior with local microstructure and microchemical composition, high resolution transmission electron microscopy (HRTEM) and energy-dispersive X-ray spectroscopy (EDS)/scanning TEM (STEM) analysis were performed near local microstructural heterogeneities (i.e., DCs). Changes to the local electrochemical behavior of irradiated and deformed microstructural heterogeneities revealed an increase in corrosion susceptibility near DCs. Corrosion potential and current revealed a considerable increase in the irradiated regions of the specimen. The role of irradiation and deformation on changes to the electrochemical behavior is related to the energy landscape of microstructural defects and their impact on charge transfer reaction kinetics.

2. Experimental

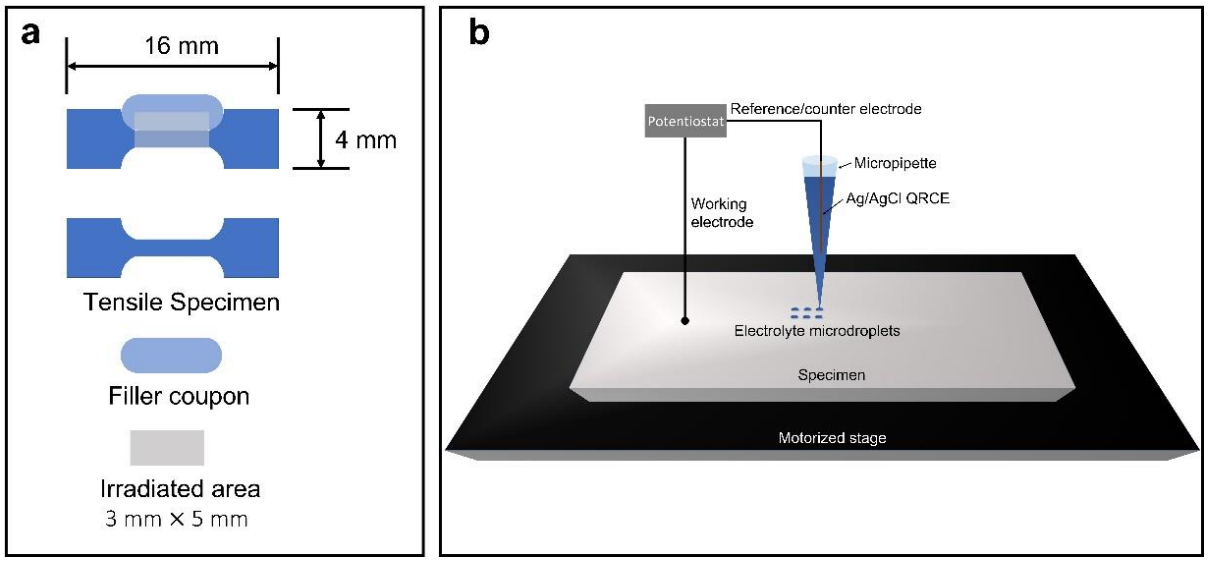

Figure 1. (a) Geometry of the tensile and filler coupon specimen and their arraignment during the irradiation procedure. (b) Schematic of the electrochemical micro-cell setup.

Sample preparation: Hot rolled 304L stainless steel (ArcelorMittal) with the nominal composition listed in **Table 1** was used to fabricate two tensile specimens and a filler coupon specimen as seen in **Figure 1a**. The specimens were polished using 50nm colloidal silica as the final polishing step. The irradiation procedure only targeted a portion of the specimen as illustrated in Figure 1A. A tensile specimen along with the filler coupon specimen were irradiated at 300 ℃ using 2 MeV proton [H^+] beam to a target fluence of 1.84×10^{19} ions/cm^2 or 1.1 dpa (flat region). The tensile specimen was

further deformed to 1% strain after ion irradiation. Another tensile specimen was irradiated at 300 ℃ using 6 MeV [Fe^{++}] to a target fluence of 2×10^{16} ions/cm^2 or 5 dpa (flat region). The specimen identification with their respective preparation history is summarized in Table 2.

Table 1. The chemical composition of the 304L stainless steel used (mass %).

Fe	Cr	Ni	Mo	Mn	N	C	Si
bal.	18.29	8.02	0.07	1.28	0.05	0.02	0.45

Table 2. Specimen identity and their respective processing conditions

Specimen identity	Flux (ions/cm^2)	Dose (dpa)	Ion source	Energy (MeV)	T (℃)	Strain (%)
H+1% ε	1.84×10^{19}	1.1	H^+	2	300	1%
H+	1.84×10^{19}	1.1	H^+	2	300	None
Fe++	2.0×10^{16}	5.0	Fe^{++}	6	300	None

Microstructure characterization: The microstructure and surface features of the specimen were determined using scanning electron microscopy (SEM, FEI Nova Nano 230) at 10 KeV accelerating voltage. Backscattered electron SEM (BSE-SEM) was used to utilize electron channeling contrast to reveal the microstructure of the specimen. Secondary electron SEM (SE-SEM) was used to distinguish surface features after deformation. A Nova 600 SEM/FIB system was used to prepare electron transparent cross-sectional lamella for transmission electron microscopy (TEM) sample preparation. A FEI Titan 300KV scanning transmission electron microscope (STEM) equipped with an Oxford Instruments EDS system was used for microstructural and elemental analysis. The surface topographies were examined using a Zygo NewView 8200 vertical scanning interferometry (VSI). A 100× (numerical aperture, NA = 0.85) interferometric objective with spatial resolutions (i.e., single pixel size in *x* and *y* directions) of 80 nm and vertical (height) resolution of both on the order of 2 nm was used. The surface topography analysis is performed with Gwyddion, v2.54.

Electrochemical analysis: An electrochemical micro-cell based on glass microcapillary filled with electrolyte solution was used to evaluate the local electrochemical behavior of the specimens using a scanning electrochemical microscopy (SECM) setup on a HEKA ElProScan instrument. The tests were performed with the micropipettes (2-4 μm opening at the tip) filled with 20 mM LiCl + 5% HNO_3 and 640mM LiCl + 5% HNO_3 solutions. N.B., the LiCl as a potential coolant contaminant, was used herein to promote measurable corrosion current signals; and the 5% HNO_3 was used to reveal corrosion resistance of only the barrier oxide film with surface hydroxides readily dissolved. During scanning, the specimen was connected to the working electrode and an AgCl-coated silver wire was inserted in the micropipette to serve as the quasi-reference-counter-electrode (QRCE). As the micropipette approached the steel surface, a 30s open circuit hold was performed allowing microdroplets to stabilize and the open circuit potentials (OCP) was measured at the end of the hold. Thereafter, potentiodynamic (PD) polarization was performed at -0.25 V_{OCP} to 0.25 V_{OCP} with a 10 mV/s scanning

rate. Electrochemical impedance spectroscopy (EIS) was conducted at OCP with ± 10 mV stimulus potential over the frequency range of 10 kHz to 1 Hz. A programmable 3D motor with nanometer precision controlled the positioning of the micropipette to create local electrochemical micro-cells measurement that was superimposed on light microscope imaged areas. A schematic of the electrochemical setup is depicted in Figure 1b.

All experiments were performed at room temperature (23 ± 2°C). All chemicals used in this study were ACS reagent grade. Solutions were prepared with deionized (DI) water (>18 MΩ-cm^2).

3. Results and discussion

3.1 Microstructural analysis

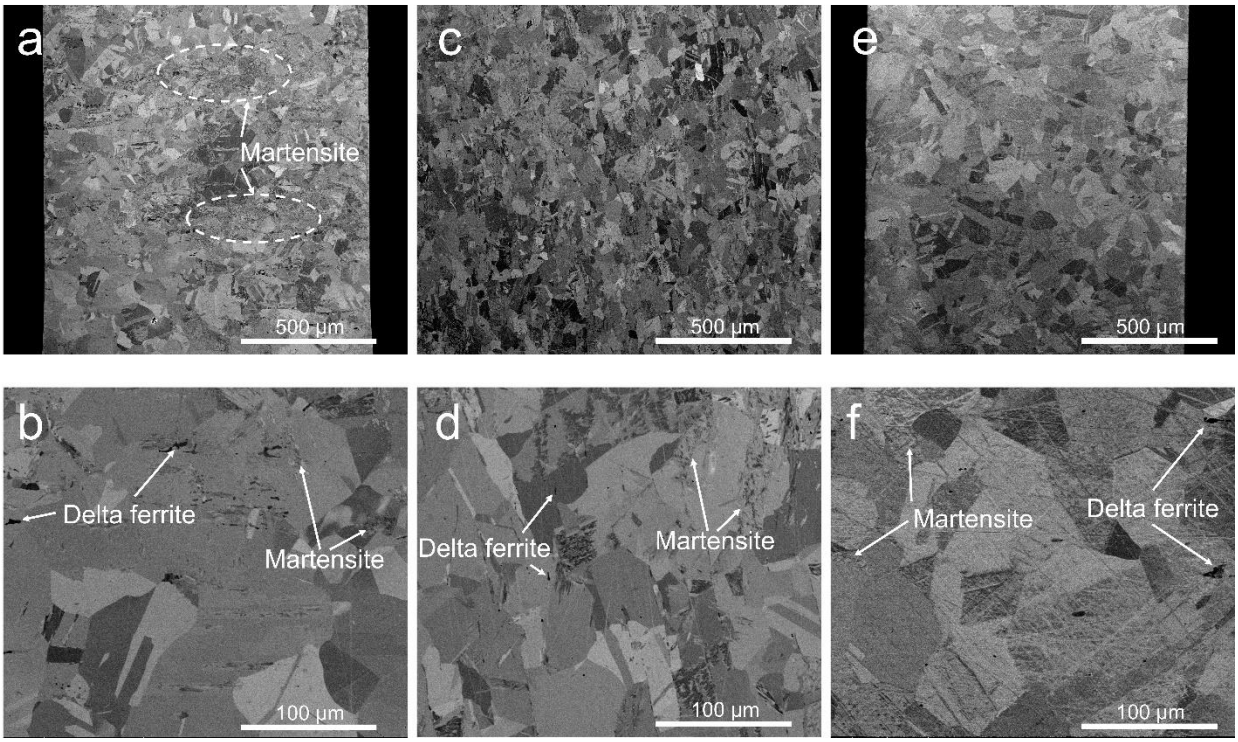

Figure 2. BSE-SEM micrographs depicting the grain geometry and microstructures of (a),(b) irradiated and deformed H+1%ε, (c),(d) irradiated H+, (e), and(f) irradiated Fe++ specimens.

The microstructure of the three specimens is revealed via BSE-SEM micrographs as shown in Figure 2. The microstructure of these specimen consists of austenite, martensite, and a small fraction of delta ferrite phases. Annealing twins can be seen across the microstructure within the austenitic matrix. The microstructure of H+1% ε consists of mostly austenite grains with grain diameter of 80 ± 41 µm with a non-uniform distribution of martensite phase (likely including strain-induced martensites) and a small

fraction of delta ferrite grains (presents in as-received condition, Figs. 2a and 2b). The microstructure of the H+ specimen (Figs. 2c and 2d) contains a small fraction of martensite phases and delta ferrite grains along the GBs and austenite grains with diameter of 42 ± 24 μm. Microstructure of Fe++ is similar to the H+1% ε specimen with grain diameter of 68 ± 35 μm.

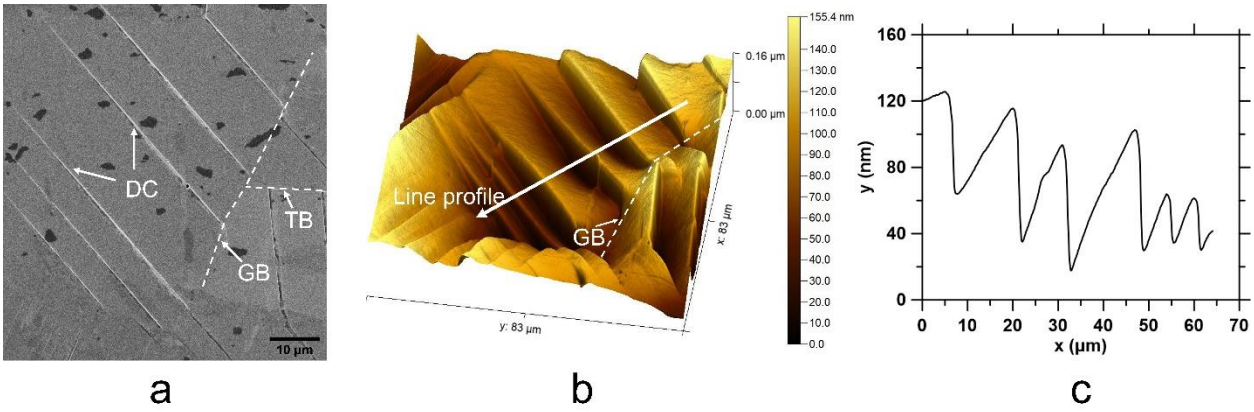

Figure 3. Appearance of DCs in irradiated and deformed 304L. (a) SE-SEM micrograph revealing DCs intersecting a GB (b) 3-D VSI mapping of DCs showing a variation in height of DCs as they approach GBs (c) line profile from the corresponding DCs having a serrated structure.

Typical surface morphology of the gauge region of the irradiated and deformed H+1% ε specimen revealed localized deformation in the form of DCs (shown in Figure 3). SE-SEM micrograph shown in Figure 3a reveals multiple DCs intersecting GBs and twin boundaries (TB). DCs that have emerged from a GB onto the surface are often terminated at another GB with average height of 33 ± 16 nm and average spacing of $11 \pm 8\ \mu m$ as measured from the height profile from the VSI maps. The height of DCs varies across a single channel with maximum height attained near the midpoint of the channel as seen in three-dimensional (3D) VSI map in figure 3b. The line profile spanning across multiple DCs within one grain is shown in figure 3c where an acute angle is formed between a pair of DCs creating wedge-like geometry. The surface of the steps between two DCs adjacent to the intersecting grain boundary (GB) appeared to be highly curved/distorted (Fig. 3b, 3c).

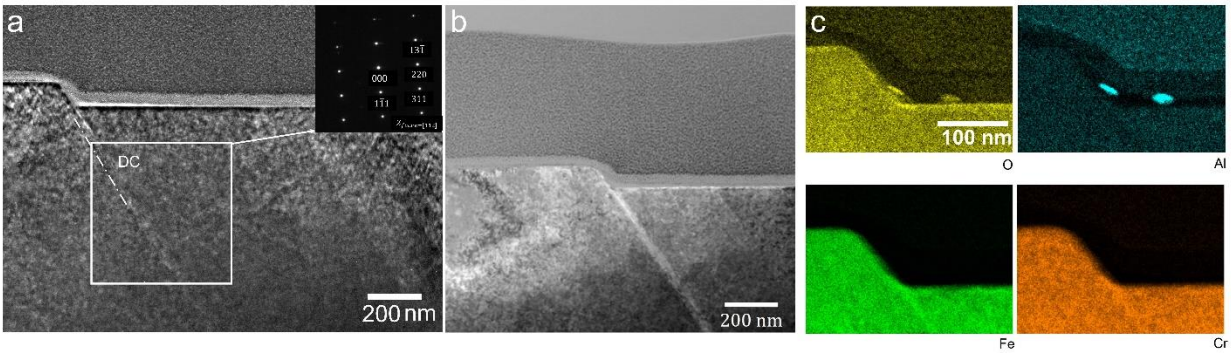

Figure 4. Cross-sectional TEM analysis and elemental mapping of irradiated and deformed 304L. (a) TEM micrograph showing a DC protruding the surface and the corresponding SAED pattern, (b) dark-field STEM micrograph revealing a change in contrast along the DC, (c) STEM-EDS elemental mapping of O, Al, Fe and Cr showing variation in thickness of the O and Fe rich surface oxide layer.

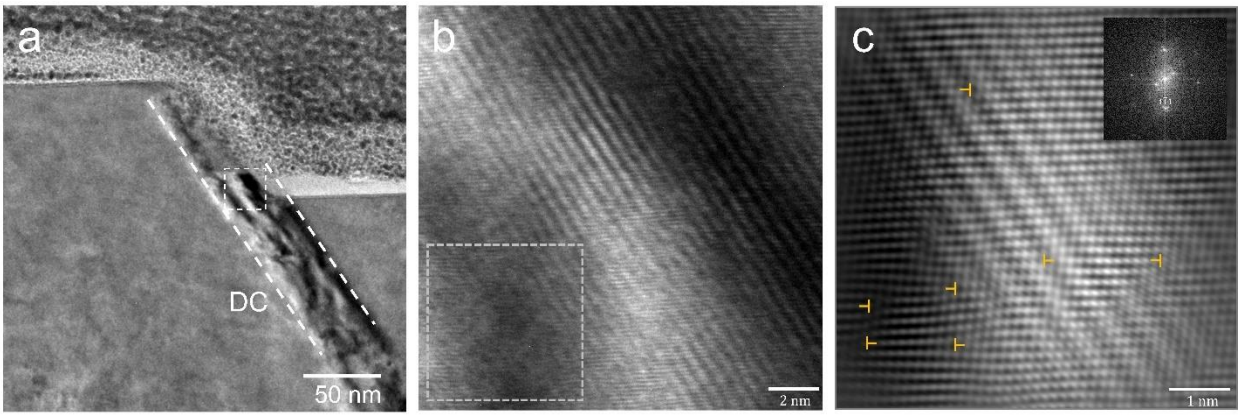

Figure 5. Cross-sectional TEM analysis of irradiated and deformed 304L. (a) TEM micrograph containing a DC slightly tilted from the $[\bar{1}12]$ zone axis, (b) close-up view of the DC region highlighted by the white square in (a), and (c) close-up view of the region highlighted by the square in (b) along with the FFT in the inset revealing edge dislocations on the $\{\bar{1}11\}$ planes.

Cross-sectional TEM, STEM and EDS micrographs of the proton irradiated and deformed 304L are depicted in Figure 4. Figure 4a shows a bright-field TEM image of the specimen tilted to $[\bar{1}12]$ zone axis according to the SAED pattern as inset. A DC with the step height of 93nm was identified parallel to the $\{13\bar{1}\}$ planes (Fig. 4a). Evidence of changes in the defect content or local misorientation variation is revealed by the contrast along the DC volume in the dark-field STEM image (Figure 4b). O- EDX map reveals a thin oxide layer around 8 nm thick on top of the SS substrate. Comparing the Fe and Cr-maps, this oxide layer seems to be rich in Fe. Notable, two small particles rich of O and Al have been identified, presumably Al_2O_3 powders retained from the polishing process.

Figure 5 shows the cross-sectional TEM analysis of the DC region oriented close to the [011] zone axis. The bright-field TEM image (Fig. 5a) reveals the DC is around 50nm in width. Figure 5b is a higher resolution of TEM image of the DC region

highlighted by the white square in Figure 5a that reveals a highly distorted lattice within the DC. A Fourier filtered atomic resolution TEM image (Fig. 5c) reveals significant number of edge dislocations on the $\{1\bar{1}1\}$ planes as confirmed by the fast Fourier transform (FFT) as the inset. The localization of deformation within the DC has caused shear induced distortion which is accommodated by the storage of dislocations; whereas the less deformed matrix is appears to contain only irradiation induced defects such as dislocation loops and point defect clusters (not analyzed here).

3.2 Electrochemical characterization

Local potentiodynamic polarization and EIS tests reveal electrochemical behavior of the irradiated and unirradiated regions of the same specimen, and can probe corrosion contributed by DCs in the irradiated and deformed regions (Figure 6). The regressed Tafel coefficients are summarized in Table 2. The value of corrosion potential (E_corr) is a mixed potential with its value depending on the rate of cathodic and anodic reactions. When the corrosion cell involves one dissolution reaction (e.g. $Fe \rightarrow Fe^{2+} + 2e^-$) and one cathodic reaction (e.g. $2H^+ + 2e^- \rightarrow H_2$), the E_corr will be between the reversable potentials of the two half reactions. At E_corr, the total oxidation and reduction current densities are equal, and the surface redox reactions attains kinetic equilibrium. A higher value of E_corr was observed of the 1.1 dpa and 5 dpa specimens as compared to the unirradiated ones. The value of E_corr increased by 0.044 V vs. Ag/AgCl and 0.018 V vs. Ag/AgCl when comparing the irradiated and unirradiated regions of H+ and Fe++ specimens, respectively. Since the electrolyte chemistry is assumed to be constant during the measurements, changes to the electrode potential are likely caused by the enhancement in hydrogen evolution reaction (HER) conducted by the passivation layer. This is evidenced by the right-shift of the cathodic curves shown in Figs. 6d and 6e. Concurrently, the values of corrosion current density (i_corr) increased by 0.37 μA/cm^2 and 1.1 μA/cm^2 in the irradiated regions of H+ and Fe++ specimen when compared to the unirradiated counterpart, respectively. This increase in HER rate after irradiation is a direct indication of induced surface reactivity due to passivation deficiency. Indeed, comparing the Nyquist plots of the irradiated and the unirradiated H+ and Fe++ reveals a decrease in impedance after irradiation for both H+ and Fe++ specimen (see Fig. 6a and 6b).

Table 3. Tafel parameters of the unirradiated, irradiated and deformed 304L specimens

	E_Corr (V vs. Ag/AgCl)	i_corr ($\mu A/cm^2$)	β_a (V/dec)	β_c (V/dec)
H+ unirr	0.277 $\pm$ 0.009	5.60 $\pm$ 1.65	0.113 $\pm$ 0.008	-0.079 $\pm$ 0.004
H+ 1.1 dpa	0.321 $\pm$ 0.013	5.97 $\pm$ 1.07	0.094 $\pm$ 0.016	-0.076 $\pm$ 0.002
Fe++ unirr	0.249 $\pm$ 0.006	1.89 $\pm$ 0.27	0.111 $\pm$ 0.006	-0.078 $\pm$ 0.004
Fe++ 5dpa	0.267 $\pm$ 0.004	2.99 $\pm$ 0.72	0.101 $\pm$ 0.012	-0.070 $\pm$ 0.002
H+1% ε DC	0.099 $\pm$ 0.021	7.18 $\pm$ 1.32	0.084 $\pm$ 0.008	-0.083 $\pm$ 0.011
H+1% ε Matrix	0.126 $\pm$ 0.0132	4.06 $\pm$ 0.77	0.110 $\pm$ 0.021	-0.094 $\pm$ 0.004

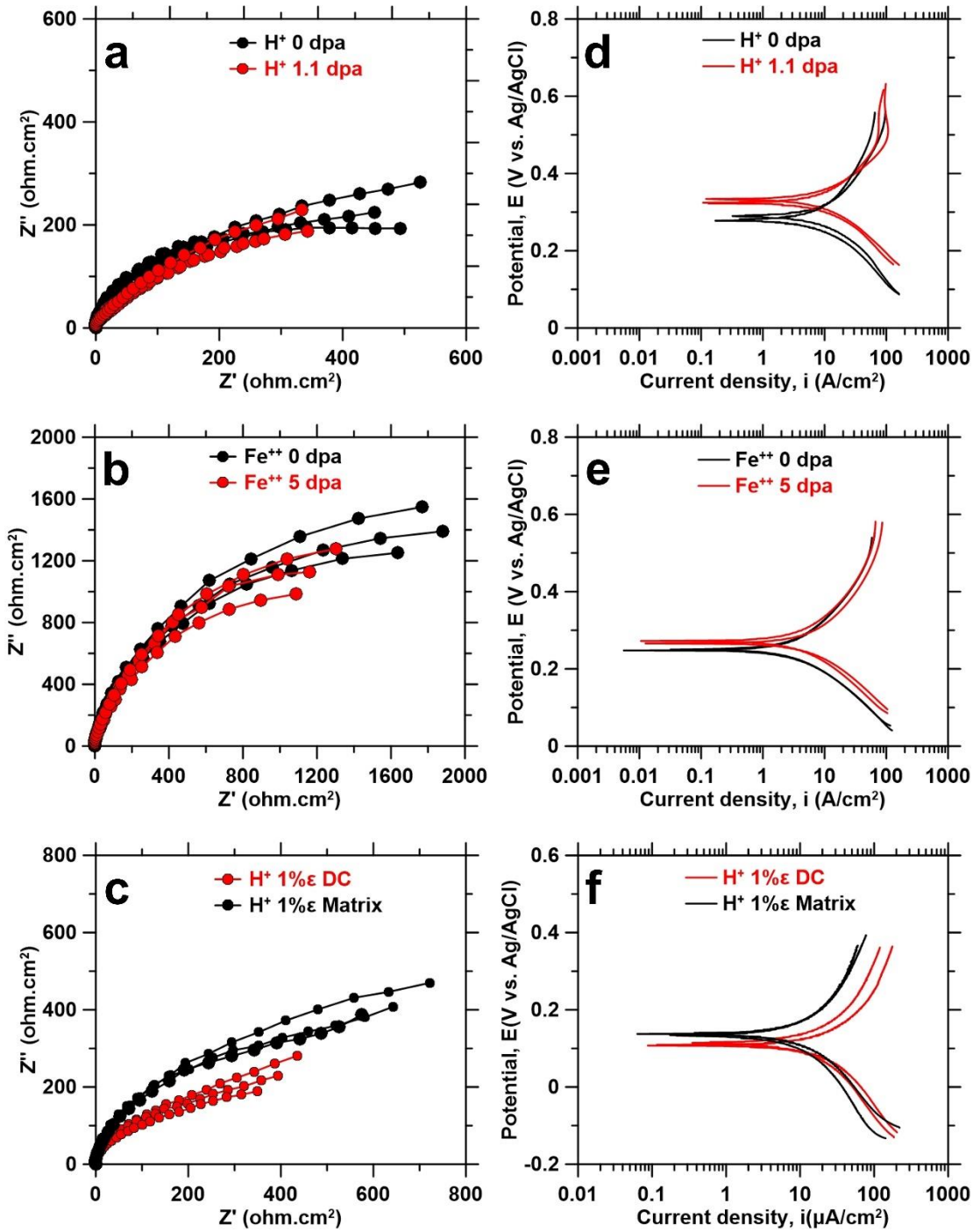

Figure 6. Electrochemical behavior of irradiated, and irradiated and deformed 304L. (a), (b) Nyquist plots of irradiated and unirradiated H+ and Fe++ specimens, respectively. (d), (e) Tafel plots of irradiated and unirradiated H+ and Fe++ specimens, respectively. (c), (f) Nyquist and Tafel plots corresponding to electrochemical micro-cells coinciding DCs and DC free deformed matrix of H+1%ε specimen, respectively.

When the test was performed on DCs, the value of E_corr was reduced by 0.027 V vs. Ag/AgCl compared to the austenite matrix without DCs for the deformed H+1% ε specimen. This is due to the i_corr increases significantly by 3.12 $\mu A/cm^2$ on DC containing electrochemical microcells when compared to the deformed austenite matrix without DCs. In this case, the anodic curves show an increase in current density with the applied potential for the DCs and intersect with the cathodic curves at lower potentials (Fig. 6f). In addition, Nyquist plots of the DCs reveals significant decreases in impedance for the regions containing DCs (Fig. 6c), likely due to local passivation breakdown and active dissolution of DCs.

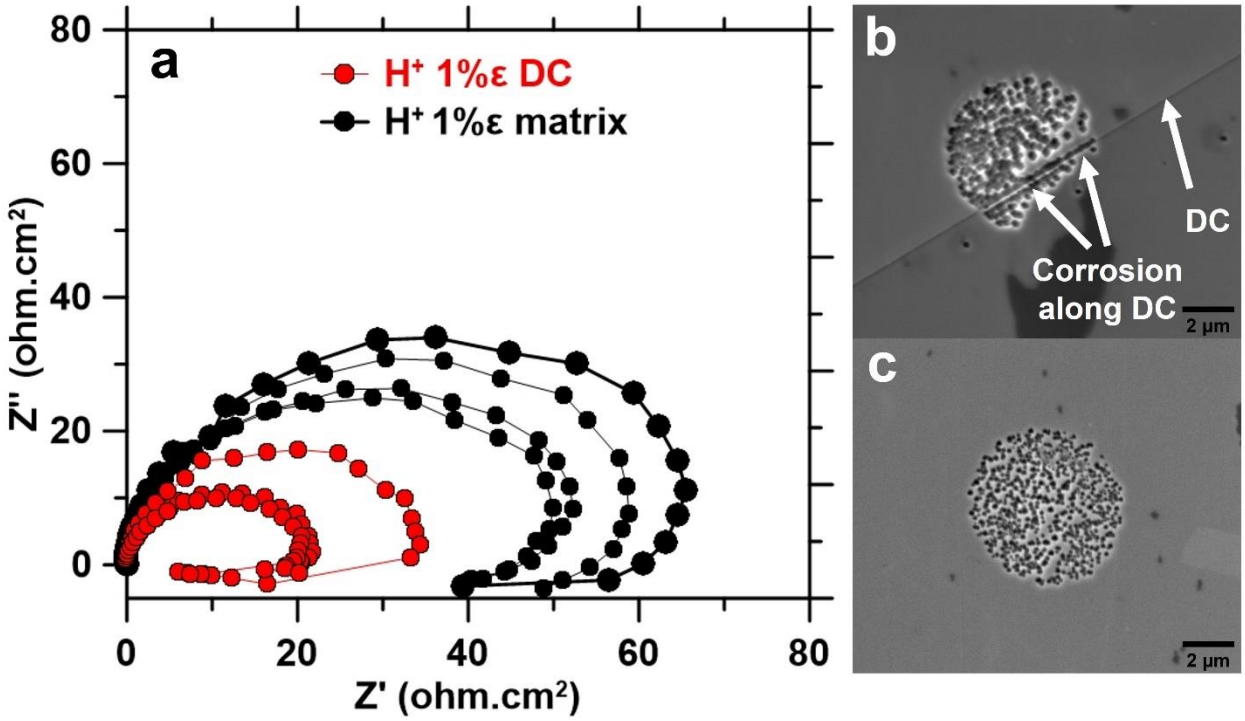

Figure 7. Local electrochemical testing and the corresponding surface topography comparing irradiated and deformed 304L tested with Cl^- concentration of 640mM for electrochemical micro-cells coinciding regions with and without DCs. (a) Nyquist plots showing reduction in impedance for micro-cells coinciding regions with DCs, (b) SE-SEM micrograph of corrosion pits formed preferentially along a DC, and (c) SE-SEM micrograph of corrosion pits formed uniformly on the austenite matrix without DCs.

To amplify the sensitivity of the microstructural defects and to reveal corrosion within the accelerated timescale, local EIS measurements was performed on regions containing DC using an electrolyte with higher Cl^- ion concentration of 640mM (proven to trigger instant corrosion). The corresponding Nyquist plots along with the SE-SEM micrographs of irradiated and deformed H+1% ε specimen with regions containing DCs and regions free of DCs are depicted in Figure 7. Low impedance compared to the experiments performed using 20mM Cl^- ion concentration as well as the corresponding corrosion pits observed in SEM micrographs indicate that passivation layer was broken, and active and pitting corrosion were taking place (Fig. 7). Regions containing at least

one DC shows a corresponding reduction in impedance as opposed to the irradiated and deformed matrix without DCs (Fig. 7a), consistently, the corresponding SE-SEM images shows preferential pitting along the DC signifying greater tendency to active corrosion (Fig. 7b).

3.3 Changes to the electrochemical behavior post irradiation

Changes in the electrochemical behavior of stainless steel after irradiation was observed using local electrochemical measurements. Increase in corrosion current, decrease in anodic and cathodic slopes and increase in the corrosion potential were observed for 304L SS irradiated to 5dpa using Fe^{++} ions and 1.1dpa using H^{+} ions. Post-irradiated specimen showed a reduction in impedance at 1Hz. The increase in the corrosion current after irradiation is correlated with the observed decrease in the impedance from the Nyquist plots presented in Figure 6.

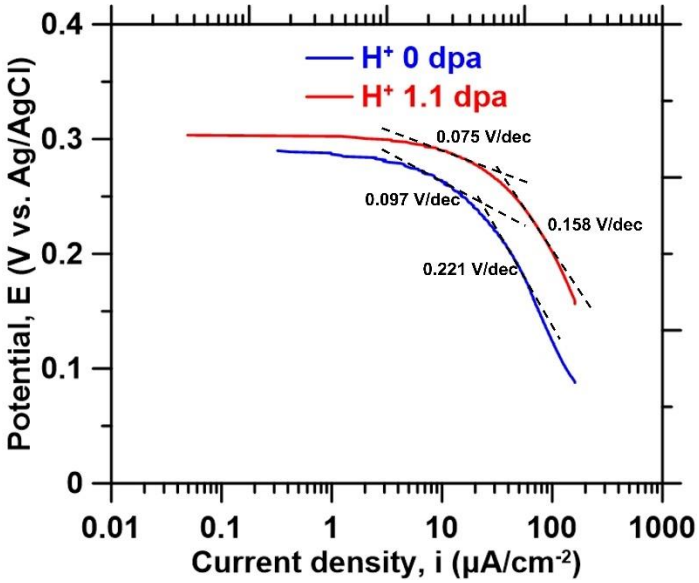

Figure 8. Cathodic Tafel slope analysis comparing the changes to the cathodic slope evolution for the irradiated and unirradiated H+ specimen. The measured cathodic Tafel slopes decreases after irradiation indicating higher kinetics of HER in the irradiated condition.

Exchange current density (i.e., i_corr) and Tafel slopes are descriptors of the reaction kinetics at the surface of the electrode [10]. An increase in exchange current density or a decrease in Tafel slopes indicated an increase in the kinetics of the reaction. [11,12]. As seen in Figure 8, the cathodic slopes differentiated at both lower and higher cathodic potentials, show both a decrease in the cathodic slope and increase in current density after irradiation. The changes in the cathodic Tafel slope with the applied overpotential was used to determine the rate determining step and the potential dependent coverage of intermediate species[10]. Presence of two cathodic slopes, one at low overpotential (i.e., 0.097 and 0.075 V/dec) and one at higher overpotentials (i.e., 0.221 and 0.158 V/dec) in acidic environments is a suggestion that the kinetic rate

determining step was controlled by the Volmer-Heyrovsky mechanism for HER, where the increase in surface coverage by hydrogen ions increases with increase in cathodic overpotential [10,13]. The decrease in cathodic slopes after irradiation suggests increase in the efficiency of the electrochemical process due to the microstructural modifications induced by the irradiation defects. Irradiation-induced surface inhomogeneities such as point defect clusters, lattice distortions, emergence of edge and screw dislocations, grain and phase boundaries are known active centers for crystal dissolution and other preferred sites for hydrogen ion adsorptions, avails easier charge transfer with the metal. Moreover, based on the jellium-dipole model[14], lattice defects such as dislocations, grain boundaries, stacking faults, and point defects often result in a change in the electron density at the defect vicinity compared to the pristine matrix, directly influences the interaction of the metal with the electrolyte, likely leading to a decrease in protection of the passive films[14–16]. These changes to the energetic landscape in the vicinity of the irradiation induced defects are directly embodied by the increases in E_corr and i_corr (Tabe 3) and decreases in the surface impedance (Figure 6).

3.4 Electrochemical behavior post irradiation and deformation

Local electrochemical measurements that were performed on regions coinciding DCs showed further increase in corrosion current, decrease in cathodic and anodic slopes and a decrease in corrosion potential. As shown in Figure 5, the DC's lattice was highly distorted with many edge dislocations identified. Dilatational strain induced by the dislocations in metals causes fluctuations in the magnitude of electron energy which oscillates at large distance from the dislocation as described in the treatment of the deformation potential of edge dislocations [6,18]; therefore, advent of dislocations beneath the surface causes chemical potential energy of electrons to change. For instance, the zero-charge potential of a low carbon steel under uniaxial tension in 0.1N H_2SO_4 electrolyte was shown to change by 100-160mV in the negative direction [6]. Further, as seen in the Figure 3b, the 3-D topography of the surface containing DCs reveals increase in surface curvature when two DC groups from two different grain misorientations intersect a GB. The surface curvature observed here is an indication of accumulation of dislocations and high residual stress in those regions[19]. Consequently, as seen in Table 3 and Figure 6, the i_corr increased by approximately 77%, the anodic Tafel slope reduced by approximately 24%, and the significant reduction of impedance coincides faster local electron transfer reaction kinetics in vicinity of these highly deformed regions. Moreover, the anodic dissolution of DCs was also apparent under active/pitting corrosion environment (see Figure 7), revealing enhanced reactivity in the post-irradiation deformation heterogeneities.

4. Conclusions

Utilization of local electrochemical measurement techniques for studying IASCC allows differentiating the influence of irradiation induced microstructural defects and local deformation heterogeneities on changes to local electrochemical behavior. Changes to the electrochemical behavior of irradiated metals can be better explained by the electron density distribution at the surfaces and interfaces effected by the energy landscape of dislocations, point defects. Influence of local deformation heterogeneities

(e.g., DCs) on corrosion behavior can be retraced to the lattice distortion and dislocation arrangement at local deformation sites. The results presented here bridge the changes in corrosion behavior with the passivation layer growth, breakdown, and active corrosion of nuclear alloys. These corrosion-related degradation can be correlated to the microstructural heterogeneities distribution, leading to co-detection of both electrochemical and microstructural characteristics of the irradiated and deformed stainless steel. The complex attributions toward IASCC susceptibility can be convoluted in electrochemical signals, characterized under ambient conditions within accelerated timescales. The resulting information can further elucidate on the detection, understanding, and prediction of IASCC in the LWR environment.

5. References

(1) Sadamori, K. Nuclear Power in a Clean Energy System: *Annales des Mines - Responsabilité et environnement* **2019**, *N° 97* (1), 122–126. https://doi.org/10.3917/re1.097.0122.

(2) Was *, G. S.; Busby, J. T. Role of Irradiated Microstructure and Microchemistry in Irradiation-Assisted Stress Corrosion Cracking. *Philosophical Magazine* **2005**, *85* (4–7), 443–465. https://doi.org/10.1080/02678370412331320224.

(3) Was, G. S.; Farkas, D.; Robertson, I. M. Micromechanics of Dislocation Channeling in Intergranular Stress Corrosion Crack Nucleation. *Current Opinion in Solid State and Materials Science* **2012**, *16* (3), 134–142. https://doi.org/10.1016/j.cossms.2012.03.003.

(4) Deng, P.; Peng, Q.; Han, E.-H.; Ke, W.; Sun, C. Proton Irradiation Assisted Localized Corrosion and Stress Corrosion Cracking in 304 Nuclear Grade Stainless Steel in Simulated Primary PWR Water. *Journal of Materials Science & Technology* **2021**, *65*, 61–71. https://doi.org/10.1016/j.jmst.2020.04.068.

(5) Alexander, R.; Proville, L.; Becquart, C. S.; Goryeava, A. M.; Dérès, J.; Lapointe, C.; Marinica, M.-C. Interatomic Potentials for Irradiation-Induced Defects in Iron. *Journal of Nuclear Materials* **2020**, *535*, 152141. https://doi.org/10.1016/j.jnucmat.2020.152141.

(6) Gutman, E. M. Metal Surface Charge Change Due to Deformation. *JOURNAL OF MATERIALS SCIENCE* **1996**, *31* (6), 1449–1454. https://doi.org/10.1007/BF00357852.

(7) Kiejna, A.; Pogosov, V. V. Simple Theory of Elastically Deformed Metals: Surface Energy, Stress, and Work Function. *Phys. Rev. B* **2000**, *62* (15), 10445–10450. https://doi.org/10.1103/PhysRevB.62.10445.

(8) Andresen, P. L.; Was, G. S. Irradiation Assisted Stress Corrosion Cracking. In *Comprehensive Nuclear Materials*; Elsevier, 2019; pp 190–217. https://doi.org/10.1016/B978-0-08-102865-0.00111-4.

(9) Andreatta, F.; Fedrizzi, L. The Use of the Electrochemical Micro-Cell for the Investigation of Corrosion Phenomena. *Electrochimica Acta* **2016**, *203*, 337–349. https://doi.org/10.1016/j.electacta.2016.01.099.

(10) Shinagawa, T.; Garcia-Esparza, A. T.; Takanabe, K. Insight on Tafel Slopes from a Microkinetic Analysis of Aqueous Electrocatalysis for Energy Conversion. *Sci Rep* **2015**, *5* (1), 13801. https://doi.org/10.1038/srep13801.

(11) Horváth, Á.; Nagy, N.; Vértesy, G.; Schiller, R. The Effect of Ion Irradiation on the Electron Work Function of Stainless Steel. *Materials Chemistry and Physics* **2018**, *217*, 541–546. https://doi.org/10.1016/j.matchemphys.2018.06.078.

(12) Schiller, R.; Horváth, Á. Addendum: Model to the “Phenomenology of the Effect of Ion Irradiation on the Work Function of Metals”, [Nucl. Instrum. Methods Phys. Res. Sect. B 466 (2020) 12–16]. *Nuclear Instruments and Methods in Physics Research Section B: Beam Interactions with Materials and Atoms* **2020**, *479*, 246–248. https://doi.org/10.1016/j.nimb.2020.07.015.

(13) Bhardwaj, M.; Balasubramaniam, R. Uncoupled Non-Linear Equations Method for Determining Kinetic Parameters in Case of Hydrogen Evolution Reaction Following Volmer–Heyrovsky–Tafel Mechanism and Volmer–Heyrovsky

Mechanism. *International Journal of Hydrogen Energy* **2008**, *33* (9), 2178–2188. https://doi.org/10.1016/j.ijhydene.2008.02.027.
(14) Schmickler, W. A Jellium-Dipole Model for the Double Layer. *Journal of Electroanalytical Chemistry and Interfacial Electrochemistry* **1983**, *150* (1–2), 19–24. https://doi.org/10.1016/S0022-0728(83)80185-5.
(15) Arponen, J.; Hautojarvi, P.; Nieminen, R.; Pajanne, E. Charge Density and Positron Annihilation at Lattice Defects in Aluminium. *J. Phys. F: Met. Phys.* **1973**, *3* (12), 2092–2108. https://doi.org/10.1088/0305-4608/3/12/011.
(16) Duffy, D. M.; Harding, J. H.; Stoneham, A. M. The Energies of Point Defects near Metal/Oxide Interfaces. *Journal of Applied Physics* **1994**, *76* (5), 2791–2798. https://doi.org/10.1063/1.357544.
(17) Chen, X.; Gussev, M.; Balonis, M.; Bauchy, M.; Sant, G. Emergence of Micro-Galvanic Corrosion in Plastically Deformed Austenitic Stainless Steels. *Materials & Design* **2021**, *203*, 109614. https://doi.org/10.1016/j.matdes.2021.109614.
(18) Brown, R. A. Electron Distribution about an Edge Dislocation in a Metal. *Phys. Rev.* **1966**, *141* (2), 568–572. https://doi.org/10.1103/PhysRev.141.568.
(19) Poole, B.; Dunne, F. P. E. Slip Band Interactions and GND Latent Hardening in a Galling Resistant Stainless Steel. *Materials Science and Engineering: A* **2021**, *813*, 141176. https://doi.org/10.1016/j.msea.2021.141176.
(20) Andresen, P. L.; Peter Ford, F. Life Prediction by Mechanistic Modeling and System Monitoring of Environmental Cracking of Iron and Nickel Alloys in Aqueous Systems. *Materials Science and Engineering: A* **1988**, *103* (1), 167–184. https://doi.org/10.1016/0025-5416(88)90564-2.